

Toward Understanding the Lithium Transport Mechanism in Garnet-type Solid Electrolytes: Li⁺ Ion Exchanges and Their Mobility at Octahedral/Tetrahedral Sites

Dawei Wang,[†] Guiming Zhong,[†] Wei Kong Pang,^{‡,§} Zaiping Guo,[§] Yixiao Li,[†] Matthew J. McDonald,[†] Riqiang Fu,^{*,||} Jin-Xiao Mi,[†] and Yong Yang^{*,†}

[†]Collaborative Innovation Center of Chemistry for Energy Materials, State Key Lab of Physical Chemistry of Solid Surface and Department of Chemistry, College of Chemistry and Chemical Engineering and [‡]Department of Material Science and Engineering, Xiamen University, Xiamen 361005, China

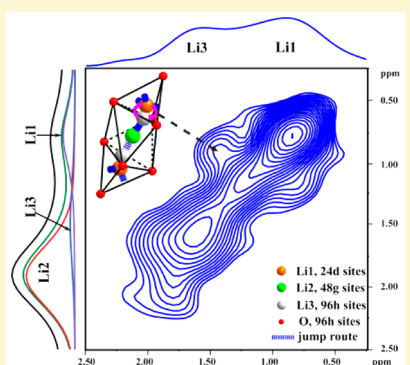
[§]The Bragg Institute, Australian Nuclear Science and Technology Organisation, Locked Bag 2001, Kirrawee DC, New South Wales 2232, Australia

[¶]Institute for Superconducting and Electronic Materials, University of Wollongong, Wollongong, New South Wales 2522, Australia

^{||}National High Magnetic Field Laboratory, 1800 E. Paul Dirac Drive, Tallahassee, Florida 32310, United States

S Supporting Information

ABSTRACT: The cubic garnet-type solid electrolyte $\text{Li}_7\text{La}_3\text{Zr}_2\text{O}_{12}$ with aliovalent doping exhibits a high ionic conductivity, reaching up to $\sim 10^{-3} \text{ S/cm}$ at room temperature. Fully understanding the Li⁺ transport mechanism including Li⁺ mobility at different sites is a key topic in this field, and $\text{Li}_{7-2x-3y}\text{Al}_y\text{La}_3\text{Zr}_{2-x}\text{W}_x\text{O}_{12}$ ($0 \leq x \leq 1$) are selected as target electrolytes. X-ray and neutron diffraction as well as ac impedance results show that a low amount of aliovalent substitution of Zr with W does not obviously affect the crystal structure and the activation energy of Li⁺ ion jumping, but it does noticeably vary the distribution of Li⁺ ions, electrostatic attraction/repulsion, and crystal defects, which increase the lithium jump rate and the creation energy of mobile Li⁺ ions. For the first time, high-resolution NMR results show evidence that the 24d, 96h, and 48g sites can be well-resolved. In addition, ionic exchange between the 24d and 96h sites is clearly observed, demonstrating a lithium transport route of 24d–96h–48g–96h–24d. The lithium mobility at the 24d sites is found to dominate the total ionic conductivity of the samples, with diffusion coefficients of $10^{-9} \text{ m}^2 \text{ s}^{-1}$ and $10^{-12} \text{ m}^2 \text{ s}^{-1}$ at the octahedral and tetrahedral sites, respectively.



1. INTRODUCTION

Solid-state batteries promise to lead the next generation of rechargeable, high energy density lithium batteries, because of their great advantages in safety and working voltage range compared to conventional liquid electrolyte lithium ion batteries, in which the intrinsic properties of liquid electrolytes plague their performance.^{1,2} Solid electrolyte is an important constituent of all solid-state batteries and determines most of their performance.³ As a result, it has attracted great interest in recent years.^{4,5} Of various solid electrolytes, the garnet-type solid electrolyte $\text{Li}_7\text{La}_3\text{Zr}_2\text{O}_{12}$ shows great prospects with regard to the development of highly safe lithium ion batteries, because of its high ionic conductivity at room temperature, in parallel with its good chemical and electrical stability.⁶

$\text{Li}_7\text{La}_3\text{Zr}_2\text{O}_{12}$ with a cubic structure was first reported by Murugan et al. as a solid electrolyte with an ionic conductivity as high as $2.4 \times 10^{-4} \text{ S cm}^{-1}$ at 22°C , achieved only in alumina crucibles.⁷ It was found that aliovalent doping at 24d (Li1) and 16a (Zr) sites could dramatically enhance the stability and ionic

conductivity of the cubic phase, using elements such as Al³⁺, Ga³⁺, Nb⁵⁺, Ta⁵⁺, Te⁶⁺, W⁶⁺, etc.^{8–11}

Therefore, an important question regarding this material is how such doping affects the ionic conductivity. To address this issue, we need to understand the states of the lithium ions at respective sites and how lithium migrates through the crystal structure. Using density functional theory, Xu et al. concluded that the Li⁺ ions jumped from one tetrahedral site to a neighboring octahedral site and then leaped forward to another tetrahedral site in the $\text{Li}_7\text{La}_3\text{Zr}_2\text{O}_{12}$ structure.¹² Some preliminary studies have also been carried out to investigate Li migration and jumping via neutron powder diffraction (NPD) in $\text{Li}_7\text{La}_3\text{Zr}_2\text{O}_{12}$, yielding a similar conclusion.^{13,14} However, Thompson et al. drew an opposite conclusion with NPD results and claimed that the ionic conductivity of $\text{Li}_7\text{La}_3\text{Zr}_2\text{O}_{12}$ trended with the occupancy of octahedral sites;

Received: June 24, 2015

Revised: September 18, 2015

Published: September 18, 2015

they deduced that the lithium jumps from one octahedral site to a neighboring octahedral site, bypassing tetrahedral sites entirely.¹⁵

Explanations of the enhanced ionic conductivity of the garnet-type electrolytes are usually correlated with the lithium stoichiometry in the compounds, although detailed transport mechanisms are seldom investigated, in particular the sitting sites of Li^+ ions as well as their mobility and rate-determining steps.^{6,12,15} Previously, we reported on the synergistic effects of Al and Te using Al_2O_3 and ZrO_2 crucibles, demonstrating that the concentration of Li sites and ion dynamics can be modulated by aliovalent ions and accurately monitored by using NPD and solid-state NMR techniques.¹⁶ In this work, we elaborate further the effects of binary aliovalent substitution on enhancing the ionic conductivity and bolstering the lithium transport mechanism in $\text{Li}_{7-2x-3y}\text{Al}_y\text{La}_3\text{Zr}_{2-x}\text{W}_x\text{O}_{12}$ ($0 \leq x \leq 1$) with a cubic garnet structure. Furthermore, we illustrate the relationship between composition, crystal structure, lithium dynamics, and ionic conductivity in the garnet-type electrolytes.

2. EXPERIMENTAL SECTION

A conventional solid-state reaction was used to synthesize the garnet-type electrolyte. The starting materials, $\text{LiOH}\cdot\text{H}_2\text{O}$, La_2O_3 , ZrO_2 , and WO_3 (purities of 95.0%, 99.99%, 99.0%, and 99.99%, respectively, all from the Sinopharm Chemical Reagent Co., Ltd.), were mixed and ground by a planetary grinder, with isopropanol used as the grinding reagent. The precursors were ground for 12 h and dried in a 120 °C box, then calcined at 800 °C for 12 h. After the second grinding and drying, the material was pressed into pellets at 2 MPa by uniaxial cold pressing. Finally, the pellets with W, covered with green constituent powder, were sintered at 1150, 1175, and 1200 °C for 12 h in Al_2O_3 crucibles. To get a pure phase with cubic symmetry, the pellet with the composition of $\text{Li}_7\text{La}_3\text{Zr}_2\text{O}_{12}$ (i.e., without W doping) was sintered at different temperatures for 36 h in an alumina crucible.

The crystal structure of the as-prepared garnet electrolyte powder was characterized using X-ray powder diffraction. A Panalytical X'Pert (Philip, Netherlands) instrument with Cu $\text{K}\alpha$ radiation was used for this purpose.

High-resolution NPD was also used to study the material, because of its high sensitivity for “light” atoms. The powders were stored and loaded into 6 mm vanadium cans in an Ar-filled glovebox, which were sealed properly in an airtight condition. The NPD data was collected using ECHIDNA, the high-resolution neutron powder diffractometer at the Australian Nuclear Science and Technology Organisation (ANSTO).¹⁷ The neutron beam wavelength was 1.62158(8) Å, determined using the La_{11}B_6 NIST standard reference material 660b. The NPD data was obtained in the 2θ angular range of 4 to 164° with a step size of 0.125°. GSAS-II was employed to perform Rietveld analysis of the obtained NPD data.¹⁸ The refining parameters that were optimized included background coefficients; zero-shift; peak shape parameters; lattice parameters; the positional parameters of Li (48g), Li (96h), and O (96h); the fractional factors of all Li, Zr, W, and O; and isotropic atomic displacement parameters (U_{iso}). During the refinement, the total occupancy of Zr and W, sharing 16a sites, was constrained to be unity, and the U_{iso} of all elements was set to be equivalent.

The density of sintered pellets was measured using the Archimedes method. Theoretical density was calculated from the lattice parameters determined by XRD. A Hitachi S-4800 scanning electron microscope was used to check the cross-sectional morphology of samples.

Measurements of ac impedance were undertaken to measure conductivity, using a Solatron 1260 impedance analyzer with the frequency range of 1 to 10⁶ Hz and an amplitude of 100 mV. The measurement cell was constructed as follows: first, silver slurry was spread onto the surfaces of pellets and cured at 600 °C for 30 min in order to vaporize any organic solvent. Next, the silver-coated pellets were placed between two pieces of steel for testing. Test temperatures

were varied from -50 to 150 °C at 20 °C intervals to study the temperature-dependent relationship. The electronic conductivity was measured by the dc polarization method, using a Solatron 1287 electrochemical analyzer with a polarization potential of 0.1 V. The holding time was 10 000 s.

The magic-angle spinning nuclear magnetic resonance (MAS NMR) technique was used to probe the local chemical environment of the atoms and to analyze the lithium dynamics of the materials. The ⁶ Li and ²⁷ Al MAS NMR spectra were gathered at Larmor frequencies of 58.9 and 104.3 MHz, respectively, on a Bruker Avance 400 NMR spectrometer with a sample spinning speed of 12 kHz. The chemical shifts of the ⁶ Li and ²⁷ Al were calibrated by using LiCl powder (0 ppm) and $\text{Al}(\text{OH})_3$ (0 ppm), respectively. ²⁷ Al MAS NMR spectra were collected using a pulse length of 1 μ s and a recycle delay of 0.1 s. ⁶ Li MAS NMR spectra were collected using a 1/4 π pulse and a recycle delay of 40 s. The saturation recovery method was used here to characterize the spin-lattice relaxation times for different lithium sites. To reduce the $\text{Li}2$ signal in ⁶ Li MAS NMR spectra, a π pulse was first applied to invert the magnetization from the +z to -z axis; then after a recovery time of 2 s at which the strong peak ($\text{Li}2$) was zero-crossing while the other signals still remained in the -z axis, due to their difference in T_1 , a 1/2 π pulse was applied to flip those signals along the -z axis into the xy plane for observation, with a recycle delay of 110 s. The ⁶ Li -⁶ Li exchange spectra were recorded after suppression of the strong peak ($\text{Li}2$), with a mixing time of 10 s. The diffusion coefficient was detected by a static 8 mm ⁷ Li probe. ⁷ Li PFG NMR spectra were collected at the Larmor frequency of 158 MHz using a 1/2 π pulse and a recycle delay of 2 s. A series of pulse field gradients between 50–400 G/cm was applied, with a duration time of 1.42 s and a diffusion time of 10 μ s.

3. RESULTS AND DISCUSSION

3.1. Crystal Structure and Morphologies. Figure 1 shows the XRD patterns of $\text{Li}_{7-2x-3y}\text{Al}_y\text{La}_3\text{Zr}_{2-x}\text{W}_x\text{O}_{12}$ ($0 \leq x \leq 1$) sintered at different temperatures. The sample with the composition of $\text{Li}_{7-3y}\text{Al}_y\text{La}_3\text{Zr}_2\text{O}_{12}$ ($y = 0.26$), sintered at 1150 °C for 36 h, shows a pure cubic structure.¹⁶ The samples with the compositions of $x = 0.25$ and 0.5 also show pure cubic structures. It was very difficult to synthesize a pure cubic phase when the W doping reached $x = 0.75$. In most circumstances, a small amount of W salts can be detected in the samples (with peaks visible at 18°). Higher sintering temperatures reduced the amount of the impurity phase, suggesting that high sintering temperatures favored the formation of solid solutions. Finally, at the composition of $x = 1$, more impurities were detected in the samples. As the substitution content increases, the lattice parameters decrease monotonically, as seen in Figure S1. In octahedral coordination, the ionic radius of Zr^{4+} is 0.72 Å and the ionic radius of W^{6+} is 0.60 Å.¹⁹ Assuming no phase transition, the monotonic decrease in lattice parameters with increasing W content indicates the successful substitution of Zr^{4+} by W^{6+} and the formation of the $\text{Li}_{7-2x-3y}\text{Al}_y\text{La}_3\text{Zr}_{2-x}\text{W}_x\text{O}_{12}$ ($0 \leq x \leq 1$) solid solutions. The samples with the same composition showed a decrease in lattice parameters when the sintering temperature increases, indicating that more Li^+ vacancies and O defects were formed in the garnet structure at higher sintering temperatures.

As alumina crucibles were used during the sintering process, it was necessary to know the content of Al and its local environment in the samples. Our NMR and EDS results show that a fraction of Al occupies the 24d sites, and the other randomly exists along grain boundaries in the form of LaAlO_3 in some batches, with an Al content of 0.2 mol for both $x = 0.25$ and $x = 0.5$. When the W content reaches $x = 0.75$, there is no Al detectable in the samples. A similar “synergistic effect” of

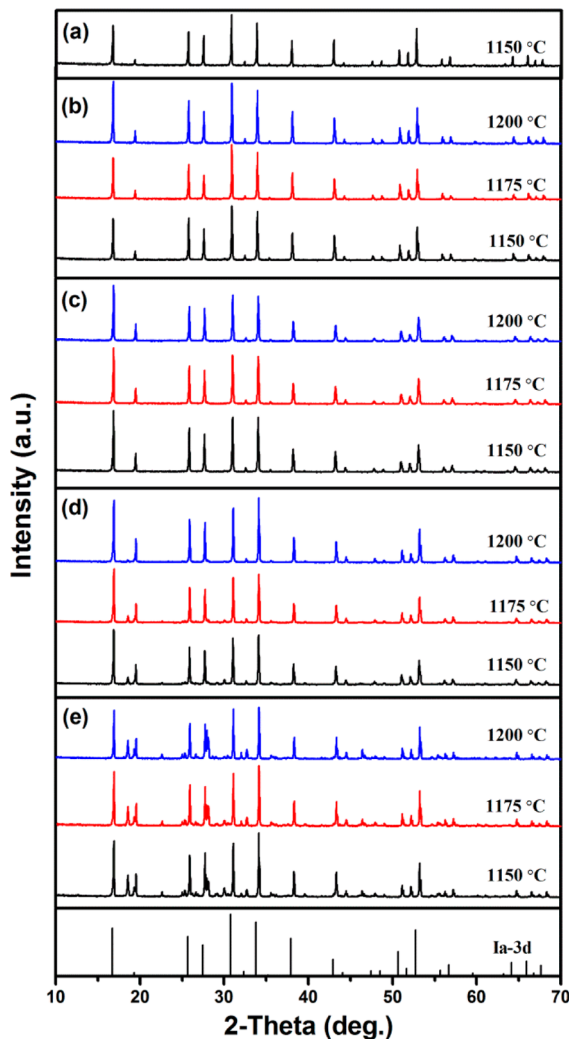


Figure 1. XRD patterns of $\text{Li}_{7-2x-3y}\text{Al}_y\text{La}_3\text{Zr}_{2-x}\text{W}_x\text{O}_{12}$ ($0 \leq x \leq 1$) sintered at different temperatures: (a) $x = 0$, (b) $x = 0.25$, (c) $x = 0.5$, (d) $x = 0.75$, and (e) $x = 1$.

Al and Te could be found in our previous study.¹⁶ Detailed information is listed in Supporting Information, Figure S2 and Table S1.

The model proposed by Goodenough and co-workers was used for the Rietveld refinement of the NPD data for the $\text{Li}_{7-2x-3y}\text{Al}_y\text{La}_3\text{Zr}_{2-x}\text{W}_x\text{O}_{12}$ ($0.25 \leq x \leq 0.75$) samples.²⁰ The W

atoms were considered to occupy the Zr (16a) sites, due to the close values of their ionic radii. However, the presence of relatively heavy La and Zr atoms in the structure complicated the refinement of the “light” aluminum and lithium atoms. Furthermore, the neutron scattering length for Al is rather low, and thus it was difficult to quantify a small concentration in the compound. With the NMR and EDS results, the Al occupancy is 0.0667 and located at the 24d sites for both $x = 0.25$ and 0.5, while the Al occupancy is 0 for $x = 0.75$. The best fits of the NPD data were obtained with the parameters listed in Table 1, and the results of Rietveld refinement are shown in Figure 2 and Figure S3.

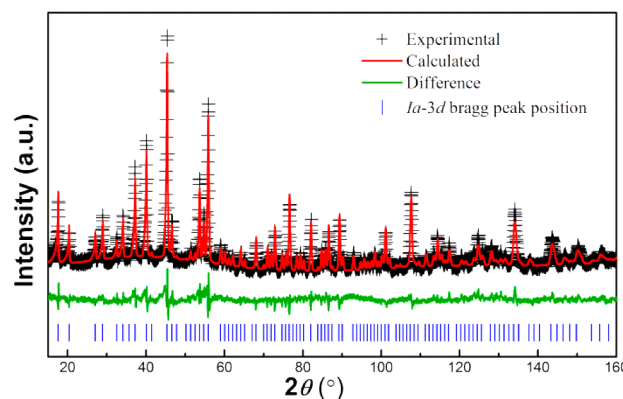


Figure 2. Rietveld refinement of the structural models, based on NPD data collected at room temperature from $\text{Li}_{7-2x-3y}\text{Al}_y\text{La}_3\text{Zr}_{2-x}\text{W}_x\text{O}_{12}$ samples with $x = 0.25$ and sintered at 1150 °C.

The lithium number is slightly higher than expected from the stoichiometry of the formula unit but still smaller than the tolerance of 7.5.²¹ The occupancy of lithium in the 24d sites ranges from 32 to 41%, and the smallest value, with $x = 0.25$, might have been due to the occupancy of Al at these sites. The Li occupancy in the 48g sites ranges from 48% to 35%, which decreases along with the total lithium content. Finally, the Li occupancy in the 96h sites remains constant. The partial occupancy of lithium at different sites might have been the reason for the observed high ionic conductivity of the $\text{Li}_{7-2x-3y}\text{Al}_y\text{La}_3\text{Zr}_{2-x}\text{W}_x\text{O}_{12}$ ($0.25 \leq x \leq 0.75$) system. In addition, oxygen defects were also detected from the Rietveld analysis.

Figure 3 shows the morphologies of the $\text{Li}_{7-2x-3y}\text{Al}_y\text{La}_3\text{Zr}_{2-x}\text{W}_x\text{O}_{12}$ samples sintered at different tem-

Table 1. Refined Structural Parameters of $\text{Li}_{7-2x-3y}\text{Al}_y\text{La}_3\text{Zr}_{2-x}\text{W}_x\text{O}_{12}$ (Space Group Ia-3d, No. 230)

stoichiometry formula	$\text{Li}_{5.9}\text{Al}_{0.2}\text{La}_3\text{Zr}_{1.75}\text{W}_{0.25}\text{O}_{12}$	$\text{Li}_{5.4}\text{Al}_{0.2}\text{La}_3\text{Zr}_{1.5}\text{W}_{0.5}\text{O}_{12}$	$\text{Li}_{5.5}\text{La}_3\text{Zr}_{1.25}\text{W}_{0.75}\text{O}_{12}$
refinement results	$\text{Li}_{6.36(12)}\text{Al}_{0.2}\text{La}_3\text{Zr}_{1.62(4)}\text{W}_{0.38(4)}\text{O}_{11.30(8)}$	$\text{Li}_{6.15(12)}\text{Al}_{0.2}\text{La}_3\text{Zr}_{1.46(6)}\text{W}_{0.54(6)}\text{O}_{11.31(8)}$	$\text{Li}_{5.76(16)}\text{La}_3\text{Zr}_{1.12(6)}\text{W}_{0.88(6)}\text{O}_{11.20(9)}$
R_{wp}	6.59%	6.70%	6.60%
lattice parameter a	12.954(1)	12.924(1)	12.900(1)
Li1 (24d)	0.32(3)	0.41(3)	0.39(3)
Li2 (48g)	0.48(2)	0.4(2)	0.35(2)
Li3 (96h)	0.21(1)	0.21(1)	0.21(1)
Al	0.067 ^a	0.067 ^a	0
La	1	1	1
Zr (R/S)	0.81(2)/0.875	0.73(3)/0.75	0.56(3)/0.625
W(R/S)	0.19(2)/0.125	0.27(3)/0.25	0.44(3)/0.375
O	0.94(7)	0.942(7)	0.933(8)

^aFixed to the same value as from the EDS results. R = refinement results; S = stoichiometry formula.

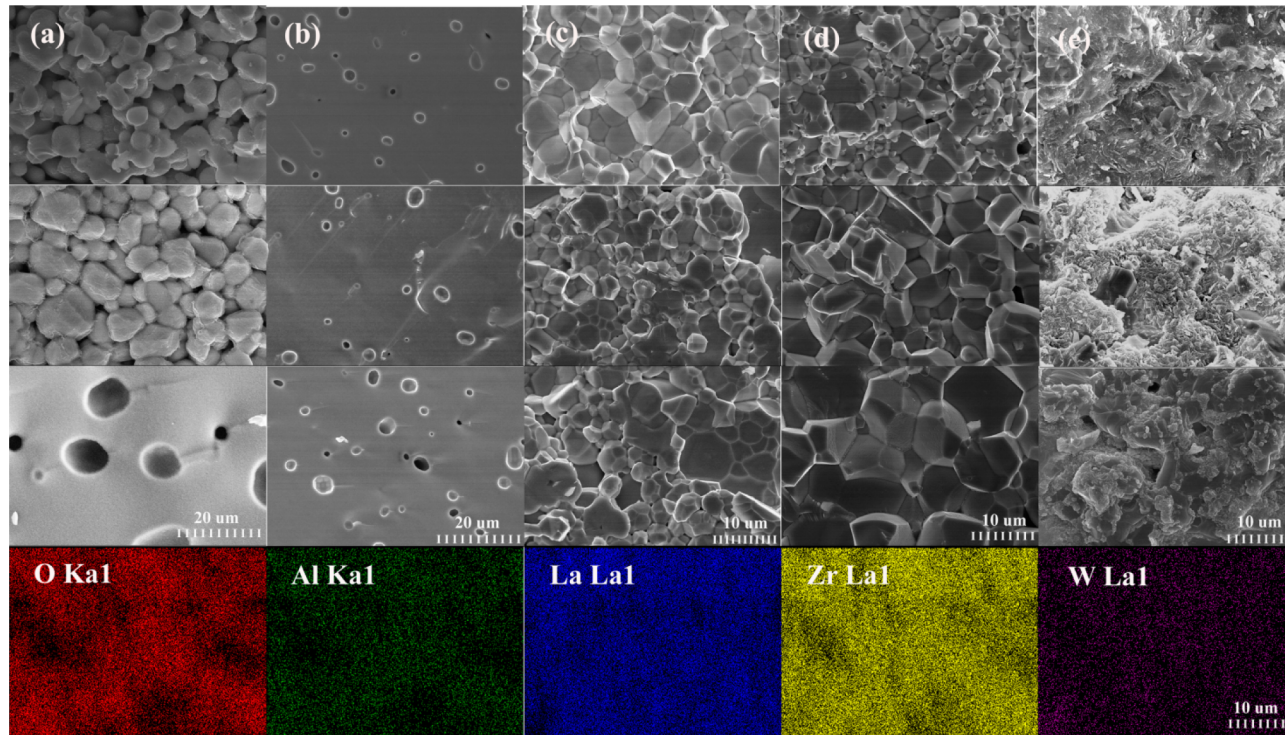


Figure 3. Morphologies of $\text{Li}_{7-2x-3y}\text{Al}_y\text{La}_3\text{Zr}_{2-x}\text{W}_x\text{O}_{12}$ ($0 \leq x \leq 1$): (a) $x = 0$, with sintering temperatures of 1000, 1100, and 1230 °C from top to bottom; (b) $x = 0.25$; (c) $x = 0.5$; (d) $x = 0.75$; and (e) $x = 1$. Sintering temperatures were 1150, 1175, and 1200 °C, from top to bottom. The EDS mappings show the elemental distribution in the sample with composition $x = 0.25$ sintered at 1150 °C for 12 h: red, O; dark green, Al; blue, La; yellow-green, Zr; purple, W.

peratures. For $x = 0$, the grains can be clearly seen in the cross sections and become larger as the sintering temperature increases. For $x = 0.25$, the grains contact well with each other, such that it is difficult to distinguish the grain boundaries in the cross sections. For $x = 0.5$, the grain boundaries can be clearly distinguished. With an increase in sintering temperature, the grains become larger, but the size of the grain is distributed inhomogeneously. For $x = 0.75$, at the sintering temperature of 1150 °C, the large grains are surrounded by many small particles. An increase in sintering temperature causes these large grains to increase in size and the small particles to vanish. By combining the XRD patterns with the SEM results, a likely explanation for this behavior is that the small particles were regions of the W-salt impurities. As the sintering temperature increased, the W-salts reacted with the samples such that the impurity content started to decrease. However, for $x = 1$, the impurities became overwhelming in quantity and thus severely interfered with the crystallization of the garnet phase. At this composition, in Figure 3, no obvious grains can be seen in the cross sections. Overall, from the morphologies of the samples, a small amount of W substitution significantly increased the sintering properties of the material. Excessive W substitution, on the other hand, gave rise to poor contact between grains. On the basis of the Li content in the samples and their morphologies, the composition of $x = 0.25$ appears to have exhibited the best ionic conductivity.²¹

Figure 3 also describes the elemental distribution at $x = 0.25$. The elements O, Al, La, Zr, and W are distributed homogeneously in the cross section, indicating the formation of solid solutions. The relative density is a key factor when evaluating the sintering properties of ceramics. Here, the relative densities of the $\text{Li}_{7-2x-3y}\text{Al}_y\text{La}_3\text{Zr}_{2-x}\text{W}_x\text{O}_{12}$ ($0 \leq x \leq 1$)

samples are between 93% and 95%, which are slightly higher than that of the sample without W substitution (Table S3). The substitution of W is an effective way to decrease the sintering requirements and increase the sintering properties.

3.2. Electrical Properties of $\text{Li}_{7-2x-3y}\text{Al}_y\text{La}_3\text{Zr}_{2-x}\text{W}_x\text{O}_{12}$ ($0 \leq x \leq 1$) Solid Solutions. Measurements of ac impedance were used to calculate the impedance and conductivity of the lithium ion conductors. Figure 4 shows the Nyquist plots of $\text{Li}_{7-2x-3y}\text{Al}_y\text{La}_3\text{Zr}_{2-x}\text{W}_x\text{O}_{12}$ ($x = 0.25$). In the case of testing temperature below 25 °C, there exists a semicircle and a curve at the high- and low-frequency sides. With an increase of testing temperature, the semicircle at the high-frequency side gradually decreases and eventually vanishes after 50 °C. This phenomenon was previously explained in the Te system.¹⁶ Two long conductive lines were used during the impedance testing, and the inductance was considered in the fitting process. When the testing temperature was below 25 °C, L(R1CPE1)(R2CPE2) as an equivalent circuit was used to fit the Nyquist plots, whereas for a testing temperature higher than 50 °C, LR1(R2CPE2) was applied, because of the vanishing of the semicircle at the high-frequency side. In these equivalent circuits, L, R1, and CPE1 represent the conductance, the total resistance of the sample, and the constant phase element of the sample, respectively, while R2 and CPE2 refer to the electrode processes. The Nyquist plots were well-fitted, and the results are listed in Table S2.

Other compositions of $\text{Li}_{7-2x-3y}\text{Al}_y\text{La}_3\text{Zr}_{2-x}\text{W}_x\text{O}_{12}$ ($x = 0.5$, 0.75, and 1) showed similar behavior (Figure S4) and were analyzed in the same way. Of particular relevance is the fact that in the $\text{Li}_{7-2x-3y}\text{Al}_y\text{La}_3\text{Zr}_{2-x}\text{W}_x\text{O}_{12}$ ($0 \leq x \leq 1$) system, the capacitance value of CPE1 was on the order of 10^{-11} to 10^{-12} F, which is the characteristic value of the bulk capacitance. This

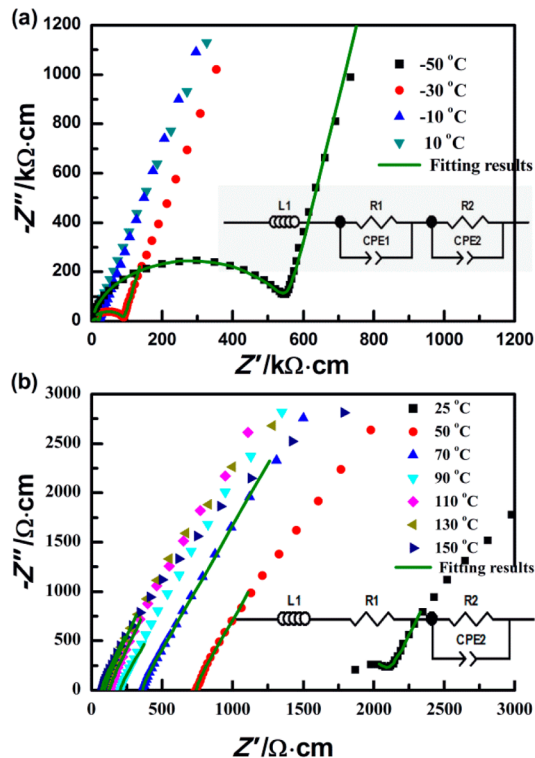


Figure 4. Nyquist plots of $\text{Li}_{7-2x-3y}\text{Al}_y\text{La}_3\text{Zr}_{2-x}\text{W}_x\text{O}_{12}$ ($x = 0.25$) sintered at 1150°C for 12 h: (a) collected at low temperature and (b) collected at high temperature.

indicates that the total resistance R_1 was dominated by the bulk resistance and the grain boundaries played a minor or negligible role in determining the total resistance. Thus, the bulk conductivity is believed to exhibit behavior similar to the total conductivity. No information regarding the grain boundary resistance could be gathered from the Nyquist plots, although the morphologies of different compositions varied. This suggests that the grain boundary properties could not be judged solely from the apparent morphologies.

Figure 5 shows the Arrhenius plots of the samples. The electrical conductivities of the W-doped $\text{Li}_{7-2x-3y}\text{Al}_y\text{La}_3\text{Zr}_{2-x}\text{W}_x\text{O}_{12}$ ($0.25 \leq x \leq 1$) are much higher than that of the pristine $\text{Li}_{7-3y}\text{Al}_y\text{La}_3\text{Zr}_2\text{O}_{12}$ ($y = 0.26$),

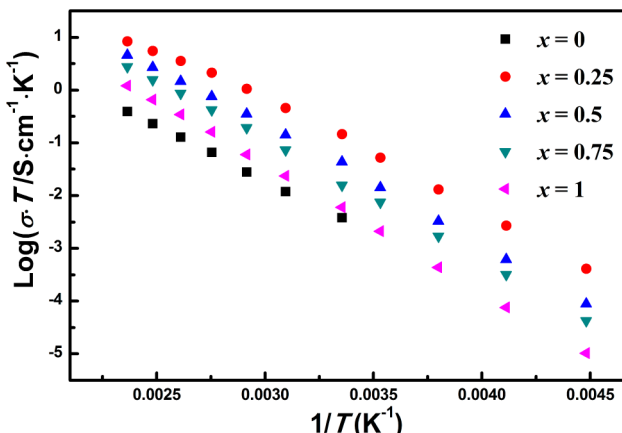


Figure 5. Arrhenius plots of $\text{Li}_{7-2x-3y}\text{Al}_y\text{La}_3\text{Zr}_{2-x}\text{W}_x\text{O}_{12}$ ($0 \leq x \leq 1$) sintered at 1150°C for 12 h.

indicating that the substitution of W greatly improves the conductivity of the garnet phase. When $x = 0.25$, the sample shows the highest ionic conductivity, $4.9 \times 10^{-4} \text{ S cm}^{-1}$ at 25°C , and lowest activation energy, 34.1 kJ/mol , although the ionic conductivity is slightly lower than that reported in the literature.¹¹ With an increase in substitution content, the conductivity decreases while the activation energy increases, a trend that also occurred previously in the Te-doped system.¹⁶ It was found that the Te played a more prominent role than Al did in determining the ionic conductivity of Al and Te codoped system in our previous study; here, the change in ionic conductivity and activation was believed to be determined by the doping of W rather than Al.¹⁶ Meanwhile, at 25°C , the Arrhenius plots show an inflection point, where the activation energy at the low-temperature side is higher than that at the high-temperature side, which might be due to the existence of an “ion-trapping effect” at low temperatures. Table S3 details the conductivities and activation energies of the $\text{Li}_{7-2x-3y}\text{Al}_y\text{La}_3\text{Zr}_{2-x}\text{W}_x\text{O}_{12}$ ($0 \leq x \leq 1$) solid solutions. Activation energies listed in Table S3 are from the high-temperature side, with the electrical properties at low temperatures being discussed in the next section. In addition, the electrical conductivities and activation energies of the garnet phases with the same composition appear to not be affected by the sintering temperature.

As a solid electrolyte used in lithium ion batteries, $\text{Li}_{7-2x-3y}\text{Al}_y\text{La}_3\text{Zr}_{2-x}\text{W}_x\text{O}_{12}$ ($0 \leq x \leq 1$) is required to be a purely lithium ionic conductor with a negligible electronic conductivity. The dc polarization method was applied to measure the electronic conductivities of the samples, as documented in Supporting Information, Figure S5. The electronic conductivities of samples are on the order of 10^{-8} to $10^{-9} \text{ S cm}^{-1}$, and the transference number of lithium is nearly unity. This demonstrates that $\text{Li}_{7-2x-3y}\text{Al}_y\text{La}_3\text{Zr}_{2-x}\text{W}_x\text{O}_{12}$ ($0 \leq x \leq 1$) were pure lithium ionic conductors and therefore suitable for lithium ion batteries.

3.3. Local Environment and Diffusion of Li in $\text{Li}_{7-2x-3y}\text{Al}_y\text{La}_3\text{Zr}_{2-x}\text{W}_x\text{O}_{12}$ ($0 \leq x \leq 1$) Solid Solutions. In the cubic garnet structure, there are 3 lithium sites, namely, the tetrahedral 24d sites and the octahedral 48g and 96h sites. The 96h sites are evolved from the distortion of 48g sites. Because the NMR technique is sensitive to the local environment, the coordination and local environment of lithium can be deduced by detecting the chemical shift of lithium. NMR measurements can also provide information on diffusion through the influence of atomic movement on the width of nuclear resonance lines and on relaxation times. In addition, an external magnetic field gradient can be used for a direct determination of diffusion coefficients.²²

Here, the ^6Li MAS NMR technique was used to check the Li^+ environment and dynamics in $\text{Li}_{7-2x-3y}\text{Al}_y\text{La}_3\text{Zr}_{2-x}\text{W}_x\text{O}_{12}$ ($0 \leq x \leq 1$). Figure 6 shows the ^6Li MAS NMR spectra of $\text{Li}_{7-2x-3y}\text{Al}_y\text{La}_3\text{Zr}_{2-x}\text{W}_x\text{O}_{12}$ ($0 \leq x \leq 1$). Two partially overlapped peaks are observed in the spectra, which are attributable to the lithium ions occupying the tetrahedral (0.8 ppm) and octahedral (1.9 ppm) sites.²³

The saturation recovery method was used to characterize the spin-lattice relaxation time (T_1). Figure S6 shows the saturation recovery of the ^6Li signals. A biexponential function fitted the data very well, as shown in the red curves, yielding two different T_1 values, as listed in Table 2. Apparently, the larger component with the shorter T_1 value (between 1.0–5.0 s) belongs to the lithium in the octahedral sites, while the

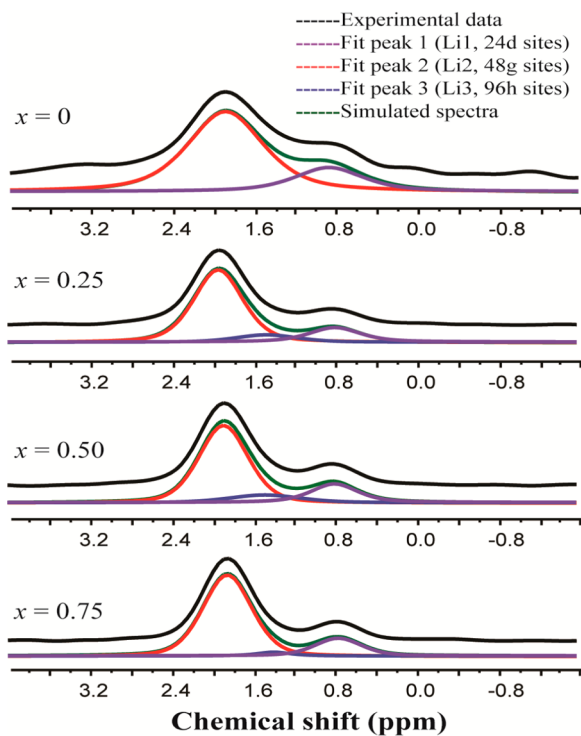


Figure 6. ${}^6\text{Li}$ MAS NMR spectra of $\text{Li}_{7-2x-3y}\text{Al}_y\text{La}_3\text{Zr}_{2-x}\text{W}_x\text{O}_{12}$ ($0 \leq x \leq 1$) sintered at 1150°C for 12 h.

smaller component with the longer T_1 value (in the range of 14–28 s) represents the lithium in the tetrahedral sites. It was also indicated that the Li at the octahedral (48g) sites with the shorter T_1 value should exhibit a higher mobility than the Li at the tetrahedral (24d) sites with the longer T_1 in our case.²²

Here we utilized the difference in T_1 to suppress the strong signals from the octahedral sites. This was done by incorporating the inversion recovery with a given recovery time, in such a way that the shorter T_1 component (i.e., the ${}^6\text{Li}$ signals from the octahedral sites) was relaxed to the null point while the longer T_1 component (i.e., the ${}^6\text{Li}$ signals from the tetrahedral sites) still remained in the $-z$ axis.²⁴ Figure 7 shows the ${}^6\text{Li}$ spectrum after suppressing the strong signals at 1.9 ppm. Interestingly, there exists an additional peak at 1.6 ppm, which is completely buried in Figure 6. This peak should have a similar T_1 value to 0.8 ppm. Because of its very weak signal intensity, this newly discovered peak at 1.6 ppm most likely belongs to those lithium ions occupying the distorted

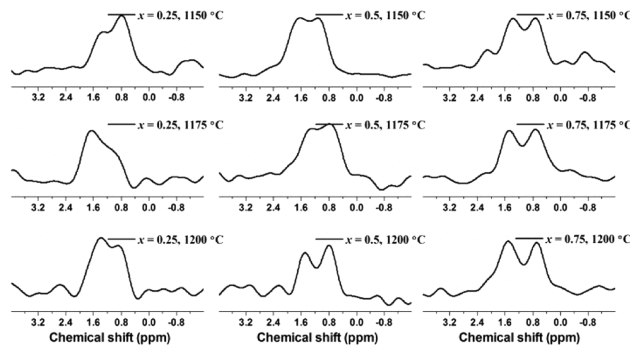


Figure 7. ${}^6\text{Li}$ MAS NMR spectra of $\text{Li}_{7-2x-3y}\text{Al}_y\text{La}_3\text{Zr}_{2-x}\text{W}_x\text{O}_{12}$ ($0 \leq x \leq 1$) gathered by incorporating the inversion recovery with a given recovery time.

octahedral sites (96h), and the peak at 1.9 ppm should belong to the lithium at the 48g sites.

With the appearance of the new peak at 1.6 ppm (96h), we deconvoluted the experimentally observed peaks with three mixed Lorentz–Gaussian peaks (Figure 6). The deconvolutions fitted well with the experimental data, yielding relative Li populations in the 24d, 48g, and 96h sites, as listed in Table 2. The integrated area corresponds to the number of lithium occupying corresponding sites; thus, the occupancies at respective sites can be obtained. It is worth noting that the peak at 1.6 ppm corresponds only to a portion of the distorted octahedral 96h sites that have a longer T_1 value. There may exist another fraction that is close to the center of the octahedral sites and has a T_1 value similar to that for the octahedral 48g sites. Those fractions would be lost during the inversion recovery time, which would have affected the fitting results, especially the occupancy of the 48g/96h sites.

The occupancy of Al at the 24d sites reduced the occupancy of Li (24d). Because the Al occupancies at the 24d sites varied with the composition x , it is not logical to discuss the occupancy of Li^+ ions at the 24d sites with x . Instead, the occupancies at the octahedral sites were directly associated with x , as Al does not occupy these sites. From the data, it is clear that, as W content increases, the Li occupancy at the octahedral 48g sites decreases, i.e., a decrease in the total Li content of the garnet structure predictably leads to a decrease in the lithium content at the octahedral sites. Both the NPD and NMR results indicated that the Li occupancy at the tetrahedral 24d sites is between 30–40% and the total amounts of Li at the octahedral sites (48g and 96h) are similar. However, the difference in 48g/

Table 2. Fitting Results of ${}^6\text{Li}$ MAS NMR Spectra of $\text{Li}_{7-2x-3y}\text{Al}_y\text{La}_3\text{Zr}_{2-x}\text{W}_x\text{O}_{12}$ ($0 \leq x \leq 1$) Solid Solutions

x	temp.	fit peak 1 (Li1, 24d sites)					fit peak 2 (Li2, 48g sites)					fit peak 3 (Li3, 96h sites)				
		c.s. ppm	L.W. (Hz)	area (%)	occu	T_1	c.s. ppm	L.W. (Hz)	area (%)	occu	T_1	c.s. ppm	L.W. (Hz)	area (%)	occu	T_1
0		0.88	46.85	22.3	0.52	1.90	51.74	77.7	0.91							
0.25	1150	0.82	35.0	15.8	0.34	23.8	1.97	35.03	79.5	0.86	4.2	1.41	36.3	0.31	0.025	
	1175	0.81	35.0	15	0.33	24.8	1.94	36.8	80.5	0.87	4.9	1.47	36.3	0.29	0.024	
	1200	0.82	36.7	16.6	0.36	22.5	1.94	40.6	81.6	0.88	4.9	1.53	36.3	0.12	0.010	
0.5	1150	0.84	31.7	17.8	0.36	28.0	1.92	33.4	73.6	0.74	2.5	1.54	34.5	0.52	0.043	
	1175	0.82	34.5	20.8	0.42	21.4	1.91	35	72.3	0.72	2.0	1.54	34.5	0.41	0.035	
	1200	0.79	31.7	15.3	0.31	17.7	1.92	33.4	75.3	0.75	2.4	1.53	34.5	0.56	0.047	
0.75	1150	0.8	32.8	17.8	0.33	24.8	1.89	33.5	76.7	0.70	1.0	1.48	38.07	0.31	0.026	
	1175	0.77	31.2	14.2	0.26	18.8	1.87	33.5	80.9	0.74	1.1	1.40	38.1	0.27	0.022	
	1200	0.79	32.8	17	0.31	14.6	1.87	31.9	76.9	0.70	0.97	1.41	32.9	0.34	0.028	

96h occupancy determined from Rietveld refinement and NMR fitting results might be due to the error associated with each method as well as the loss of a portion of the 96h sites signal from NMR fitting.

An important question regarding the lithium migration pathway is whether the Li^+ ions jump from the octahedral site to its neighboring octahedral sites, bypassing the tetrahedral sites? Or are the 24d sites in fact involved in the lithium migration pathway? In NMR, two-dimensional chemical exchange experiments can be used to measure the slow exchange between the lithium ions at the tetrahedral and octahedral sites. Unfortunately, it is extremely difficult to observe any exchange signals between the less populated lithium at the tetrahedral sites and the much more populated lithium at the octahedral sites, especially when the latter has a much shorter T_1 than the former. Again, we incorporated the inversion recovery with a given recovery time to suppress the strong signals from the octahedral sites at 1.9 ppm before doing the chemical exchange experiment. Figure 8 shows the two-

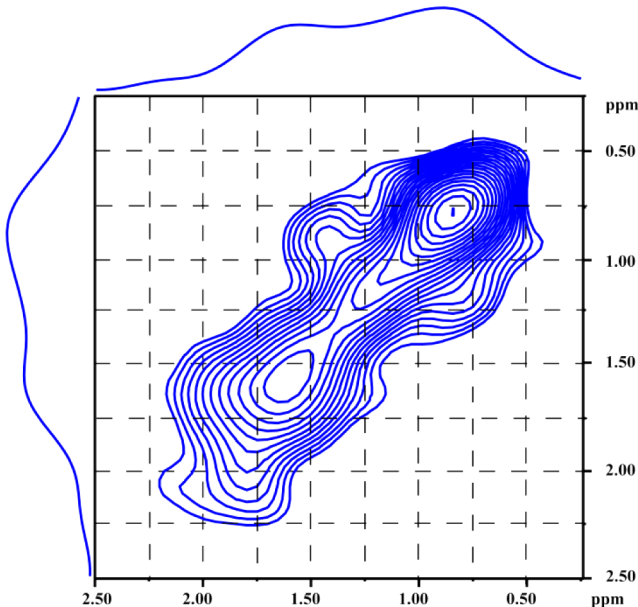


Figure 8. ${}^6\text{Li}$ - ${}^6\text{Li}$ exchange spectra of $\text{Li}_{7-2x-3y}\text{Al}_y\text{La}_3\text{Zr}_{2-x}\text{W}_x\text{O}_{12}$ ($x = 0.5$) sintered at 1150°C for 12 h.

dimensional ${}^6\text{Li}$ - ${}^6\text{Li}$ exchange spectrum after suppressing the strong signals at 1.9 ppm. Clearly, there exists a cross-peak at ($\omega_1 = 0.8$, $\omega_2 = 1.6$) ppm, indicating the correlation between the octahedral (96h) and tetrahedral (24d) sites: that is, the Li^+ ions jumped from one tetrahedral site to neighboring octahedral (96h) sites and vice versa. In the crystal structure of the garnet phase, the 96h sites are between 48g and 24d sites; this is in agreement with our deduction of lithium attribution. These results confirm that the Li^+ ions in the tetrahedral 24d sites are involved in the lithium migration pathway and support the Li^+ ions jump along 24d-96h-48g-96h-24d. Furthermore, the 24d sites exhibiting a lower mobility were expected to determine the overall conductivity.

The diffusion coefficients of $\text{Li}_{7-2x-3y}\text{Al}_y\text{La}_3\text{Zr}_{2-x}\text{W}_x\text{O}_{12}$ ($x = 0.5$) were obtained at different temperatures using ${}^7\text{Li}$ diffusion measurements. Figure 9 and Figure S7 show the decays of ${}^7\text{Li}$ intensities as a function of the applied pulse field gradient. Figure S7 clearly shows a sharp peak and a broad peak in the spectra, where the sharp peak is attributed to the Li^+ ions

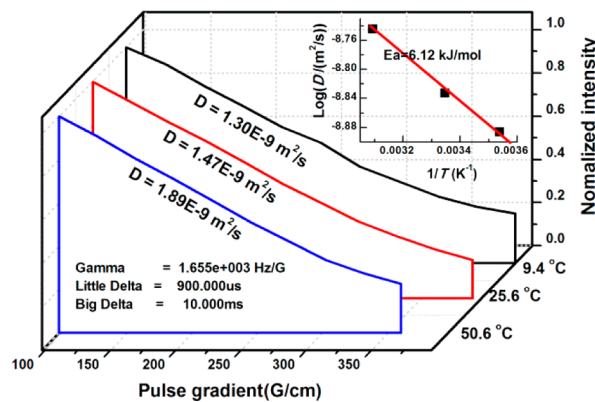


Figure 9. ${}^7\text{Li}$ PFG NMR spectra of $\text{Li}_{7-2x-3y}\text{Al}_y\text{La}_3\text{Zr}_{2-x}\text{W}_x\text{O}_{12}$ ($x = 0.5$) sintered at 1150°C for 12 h. The inset shows the Arrhenius plot of the diffusion coefficient.

occupying the octahedral sites, and the broad peak is assigned to the Li^+ ions occupying the tetrahedral sites based on their integrated areas. Clearly, the broad peak shows almost no decay within the range of the applied pulse field gradient, indicating that the Li^+ ions occupying the tetrahedral sites diffuse rather slowly. The sharp peak decays, indicating that the Li^+ ions occupying the octahedral sites diffuse fast. Fitting the data using a Stejskal-Tanner function yielded the diffusion coefficients of $1.30 \times 10^{-9} \text{ m}^2 \text{ s}^{-1}$, $1.47 \times 10^{-9} \text{ m}^2 \text{ s}^{-1}$, and $1.89 \times 10^{-9} \text{ m}^2 \text{ s}^{-1}$ at temperatures of 9.4 , 25.6 , and 50.6°C , respectively.²⁵ The diffusion coefficients obtained here characterize the diffusion rate for those Li at the octahedral sites, more precisely the 48g sites. The inset in Figure 9 shows the Arrhenius plot of the diffusion coefficient at the 48g sites, giving rise to the activation energy of 6.12 kJ/mol , which is much smaller than that from the ionic conductivity and is also much less than the activation energy of 31 kJ/mol from the average lithium jump rate that will be calculated in the next section. The average diffusion coefficient from the Nernst-Einstein relationship is on the order of $10^{-12} \text{ m}^2 \text{ s}^{-1}$, much lower than that obtained through the diffusion measurements, $10^{-9} \text{ m}^2 \text{ s}^{-1}$. Thus, we believe that the Li^+ ions should have jumped only along the 24d-96h-48g-96h-24d pathway, because any Li^+ ions jumping from one octahedral site to a neighboring octahedral site would have yielded a much higher ionic conductivity. Taking into account the lithium transport route of 24d-96h-48g-96h-24d and the fact that the mobility at the 24d sites determined the whole ionic conductivity of the sample, it is reasonable to conclude that the diffusion coefficient of Li at the 24d sites was on the order of $10^{-12} \text{ m}^2 \text{ s}^{-1}$.

3.4. Low-Temperature Properties of $\text{Li}_{7-2x-3y}\text{Al}_y\text{La}_3\text{Zr}_{2-x}\text{W}_x\text{O}_{12}$ ($0 \leq x \leq 1$) Solid Solutions.

Figure 5 shows an inflection point of the Arrhenius plot at 25°C , where the activation energy of the ionic conductivity at the low-temperature side is much higher than that at the high-temperature side, a phenomena stemming from the ion-trapping effect. For fast ion conductors, Nyquist plotting at low temperatures can show a more complete semicircle, which is necessary for the collection of microinformation.

Usually, the ac conductivity and the frequency follow Jonscher's universal power law, eq 1.²⁶

$$\sigma(\omega) = \sigma_{dc} + A\omega^n = K\omega_p[1 + (\omega/\omega_p)^n] \quad (1)$$

where σ_{dc} is the dc ionic conductivity, ω is the angular frequency, ω_p represents the jump rate of the charge carriers, A

and K are the prefactors, and n is a dimensionless frequency exponent that lies in the range $0 < n < 1$. Figure 10 shows the

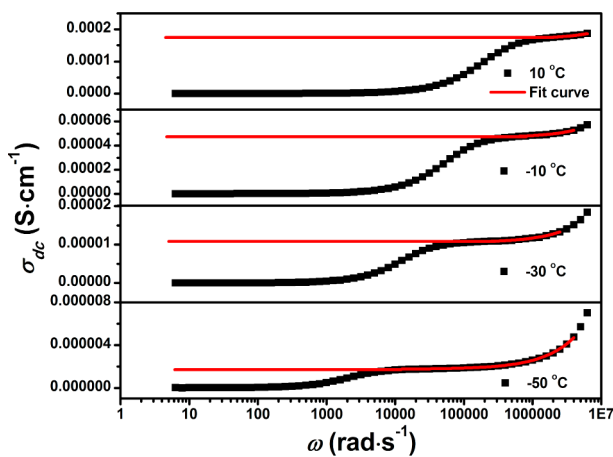


Figure 10. Frequency-dependent $\sigma(\omega)$ of $\text{Li}_{7-2x-3y}\text{Al}_y\text{La}_3\text{Zr}_{2-x}\text{W}_x\text{O}_{12}$ ($x = 0.25$) sintered at 1150°C and associated fitting results.

frequency-dependent $\sigma(\omega)$. There are two platforms in the data, with the platform at the high-frequency side representing the dc conductivity σ_{dc} and the decrease in ionic conductivity at the low-frequency side being attributed to the electrode process. Here, the bulk properties are the only focus of the fitting, and so the Jonscher relationship was used to fit the data at the high-frequency side. The intercept of the fitting curve on the y axis represents the dc conductivity, while the jump rate ω_p could be directly taken from the fitting results. The mobile ion

concentration was calculated from the Nernst–Einstein–Smoluchowski relationship, eq 2,

$$\sigma_{dc} = \frac{c\omega_p q^2 \alpha^2}{2\pi kT} \quad (2)$$

where c is the mobile ion concentration, q is the charge, α is the jump distance and set to be 2\AA , k is the Boltzmann constant, and T is the absolute temperature in degrees Kelvin. The results are listed in Table S4.

σ_{dc} , ω_p , and c are important factors when studying solid electrolytes, and their relationships with test temperatures are given in Figure 11 and Figures S8 and S9. The data fit the Arrhenius plots well, indicating a thermal activation process. The activation energies were calculated and are listed in Table 3. The sample with the composition of $x = 1$, however, shows a large amount of impurities, which greatly affects the shape of the Nyquist plot and the fitting results. For that reason, only the data gathered from compositions with $x = 0.25$, 0.5, and 0.75 are discussed.

The activation energy of the ionic conductivity at the high-temperature side in this data shows a clear pattern, but because of the ion-trapping effect, the difference in activation energy of various compositions is not as obvious at the low-temperature side. This ion-trapping effect is treated as the creation energy of mobile Li^+ ions, that is, it increases the activation energy that activates Li^+ from fixed sites to a mobile status.

With an increase in x from 0.25 to 0.75, σ_{dc} decreases from 1.7×10^{-4} to $2 \times 10^{-5} \text{ S cm}^{-1}$ (10°C), the jump rate ω_p decreases from 77 256 768 to 13 434 467 rad/s (10°C), and the mobile Li^+ concentration c decreases from 5.25×10^{21} to $3.01 \times 10^{21} \text{ cm}^{-3}$ (10°C). ω_p shows a more obvious decrease

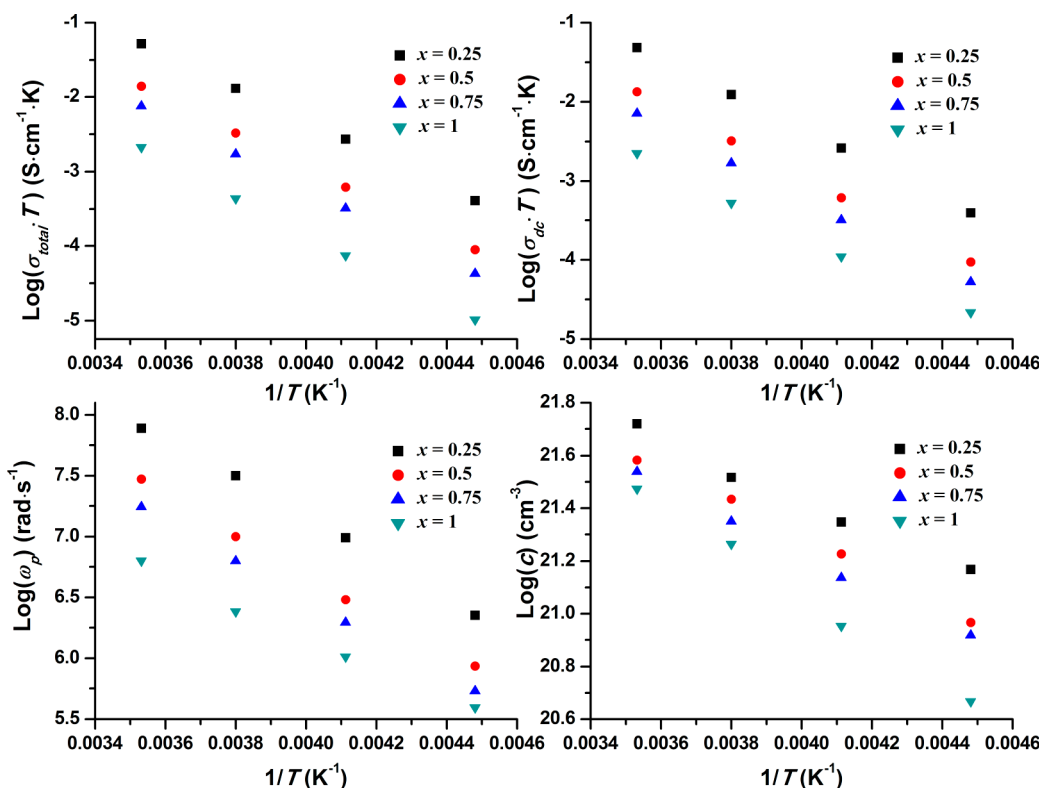


Figure 11. Low-temperature properties of $\text{Li}_{7-2x-3y}\text{Al}_y\text{La}_3\text{Zr}_{2-x}\text{W}_x\text{O}_{12}$ ($0 \leq x \leq 1$) sintered at 1150°C . σ_{total} values are the fitting results of Nyquist plots while σ_{dc} values are the fitting results of Figure 10.

Table 3. Low-Temperature Properties of $\text{Li}_{7-2x-3y}\text{Al}_y\text{La}_3\text{Zr}_{2-x}\text{W}_x\text{O}_{12}$ ($0 \leq x \leq 1$)

x	S.T.	$\sigma_{dc}/10^\circ\text{C}$ (S cm $^{-1}$)	$\omega_p/10^\circ\text{C}$ (rad s $^{-1}$)	$c/10^\circ\text{C}$ (cm $^{-3}$)	ω_0 (rad s $^{-1}$)	E_a/HT^a (kJ/mol)		E_a/LT^a (kJ/mol)				
						$E_{a,\sigma}$	$E_{a,c}$	$E_{a,\sigma}$	$E_{a,\sigma/dc}$	$E_{a,\omega}$	$E_{a,c}$	E_{tp}
0.25	1150	1.7×10^{-4}	7.73E7	5.25E21	4.47E13	34.1	2.9	42.4	42.2	31.1	11	8.1
	1175	1.37×10^{-4}	6.72E7	4.89E21	3.89E13	34.4	3.4	42.5	42.2	31	11.2	7.8
	1200	1.31×10^{-4}	1.38E8	2.27E21	2.69E13	34.8	4.4	42.7	41.9	30.2	11.5	7.1
0.5	1150	4.72×10^{-5}	2.97E7	3.81E21	1.44E13	38.9	7.9	44.5	43.5	31	12.5	4.6
	1175	4.47×10^{-5}	2.22E7	4.84E21	8.9E12	38.4	8	44.4	43.4	30.4	13	5
	1200	3.79×10^{-5}	2.29E7	3.96E21	1.2E13	39.4	8.3	44.5	43.6	31.1	12.5	4.2
0.75	1150	2.52×10^{-5}	1.75E7	3.45E21	7.2E12	41.93	11.3	45.2	43.1	30.5	12.5	1.2
	1175	2.02×10^{-5}	1.60E7	3.01E21	7.2E12	42	11.6	45.6	43.1	30.7	12.7	1.1
	1200	2.75×10^{-5}	1.34E7	4.52E21	3.8E12	41.7	10	46.5	44.9	31.6	13.2	3.2
1	1150	7.91×10^{-6}	6.35E6	2.89E21	1.6E11	43.7		46.5	40.6	24	16.5	
	1175	5.27×10^{-6}	3.22E6	3.96E21	1.3E10	44.8		47.4	40.7	19.4	21.3	
	1200											

^a $E_{a,\sigma}$ is the activation energy of ionic conductivity; $E_{a,c}$ is the creation energy of mobile Li⁺ ions; $E_{a,\omega}$ is the activation energy of jump rate; and E_{tp} is the ion-trapping effect.

compared to that of c , indicating that the decrease in ionic conductivity is mainly affected by the decrease in ω_p . However, by examining different compositions, the activation energy of the jump rate at between 30 and 32 kJ/mol shows negligible differences, indicating that the barrier for lithium jumping is not obviously changed. The decrease in the crystal lattice size is thus apparently too small to affect the activation energy of the lithium jump rate. The decrease in lithium jump rate with x is mainly due to the decrease in attempt frequency, although the structural reasons for this phenomenon are not yet very clear. At 10 °C, only about 1–10% of the total lithium is mobile in the garnet structure: most of the Li⁺ ions are fixed in the lattice and do not participate in lithium transport.²⁷ With an increase in x , the creation energy of mobile Li⁺ ions increases from 2.9 to 11.6 kJ/mol at the high-temperature side. The dissolution energy of W–O is 653.2 kJ/mol, which is smaller than the 760 kJ/mol of the Zr–O band.¹⁹ With an increase in W content, the average dissolution energies of the M–O band decrease, the O shows a stronger attraction to Li⁺, and the dissolution energy of the Li–O band increases. This causes the creation energy of mobile Li⁺ ions to increase. The activation energy of the jump rate ω_p is nearly constant. Therefore, the difference in activation energies of ionic conductivity is mainly affected by the creation energy of mobile Li⁺ ions. However, at low temperatures, the ion-trapping effect decreases from 8.1 to 1.1 kJ/mol, behavior that is mainly due to a decrease in Li⁺ ion content and crystal defects in the garnet structure. These two opposite behaviors cause the creation energy of mobile Li⁺ ions to exhibit a minor increase with x at the low-temperature side, from 11 to 13 kJ/mol. Because the lithium mobility at 24d sites determines the total conductivity, the obtained parameters are mainly attributed to the Li⁺ ions at 24d sites.

4. CONCLUSION

A series of $\text{Li}_{7-2x-3y}\text{Al}_y\text{La}_3\text{Zr}_{2-x}\text{W}_x\text{O}_{12}$ ($0 \leq x \leq 1$) solid solutions were synthesized, and their properties were studied. The sample with the composition of $x = 0.25$ showed the highest ionic conductivity, with $\sigma_{rt} = 4.9 \times 10^{-4}$ S cm $^{-1}$, and the lowest activation energy, 34.1 kJ/mol. The ionic conductivities of the solid solutions decreased with the further substitution of W, while the activation energies increased. The decrease in ionic conductivity was due to a decrease in jump rate at the 24d sites, which determined the total ionic conductivity of the samples. The increase of activation energy

was due to the heightened creation energy of mobile Li⁺ ions, and these mobile ions made up only a small amount of the total lithium. In addition, the ion-trapping effect decreased with an increase in substitution content. The aliovalent substitution of W did not seriously affect the crystal structure or the activation energy of Li⁺ ion jumping, but it noticeably varied the distribution of Li⁺ ions, electrostatic attraction/repulsion, and crystal defects, which increased the lithium jump rate and the creation energy of mobile Li⁺ ions. This is the mechanism of the previously observed effect that aliovalent substitution has on ionic conductivity.

Three lithium sites, the tetrahedral 24d as well as the octahedral 48g and 96h, were successfully resolved by high-resolution solid-state NMR, with the diffusion coefficients of lithium found to be 10^{-9} m 2 s $^{-1}$ at the octahedral sites and 10^{-12} m 2 s $^{-1}$ at the tetrahedral sites. The lithium ions exchange between the 24d sites and 96h sites was observed, which directly demonstrated a lithium transport route of 24d–96h–48g–96h–24d. The tetrahedral sites were the key points and determined the ionic conductivity of the $\text{Li}_{7-2x-3y}\text{Al}_y\text{La}_3\text{Zr}_{2-x}\text{W}_x\text{O}_{12}$ structure.

The work carried out here sets up a direct relationship between the macroscale ionic conductivity and microscale lithium dynamics, i.e., lithium jump rates and/or lithium diffusion coefficients at different sites, and provides a deeper understanding of lithium transport in the lithium-stuffed $\text{Li}_{7-2x-3y}\text{Al}_y\text{La}_3\text{Zr}_{2-x}\text{W}_x\text{O}_{12}$ structure. It is anticipated that a combination of ac impedance testing (at high- and low-temperature ranges) and the use of the solid-state NMR technique would be a powerful way to study the lithium transfer performance and could be helpful in understanding the lithium dynamics in all solid electrolytes.

■ ASSOCIATED CONTENT

S Supporting Information

The Supporting Information is available free of charge on the ACS Publications website at DOI: 10.1021/acs.chemmater.5b02429.

Lattice parameters of $\text{Li}_{7-2x}\text{La}_3\text{Zr}_{2-x}\text{W}_x\text{O}_{12}$ ($0 \leq x \leq 1$); ²⁷Al MAS NMR spectra of $\text{Li}_{7-2x-3y}\text{Al}_y\text{La}_3\text{Zr}_{2-x}\text{W}_x\text{O}_{12}$ ($0 \leq x \leq 0.75$); EDS results of $\text{Li}_{7-2x-3y}\text{Al}_y\text{La}_3\text{Zr}_{2-x}\text{W}_x\text{O}_{12}$ ($0 \leq x \leq 0.75$); Rietveld refinement of the structural models, based on NPD data from

$\text{Li}_{7-2x-3y}\text{Al}_y\text{La}_3\text{Zr}_{2-x}\text{W}_x\text{O}_{12}$ samples; Nyquist plots of $\text{Li}_{7-2x-3y}\text{Al}_y\text{La}_3\text{Zr}_{2-x}\text{W}_x\text{O}_{12}$ ($x = 0.5$ and 0.75); fitting results of Nyquist plots of $\text{Li}_{7-2x-3y}\text{Al}_y\text{La}_3\text{Zr}_{2-x}\text{W}_x\text{O}_{12}$ ($x = 0.25$); fitting results of Arrhenius plots of $\text{Li}_{7-2x-3y}\text{Al}_y\text{La}_3\text{Zr}_{2-x}\text{W}_x\text{O}_{12}$ ($0 \leq x \leq 1$); dc polarization curves of $\text{Li}_{7-2x-3y}\text{Al}_y\text{La}_3\text{Zr}_{2-x}\text{W}_x\text{O}_{12}$ ($0 \leq x \leq 1$) solid solutions; spin-lattice relaxation curves and fitting curves of $\text{Li}_{7-2x-3y}\text{Al}_y\text{La}_3\text{Zr}_{2-x}\text{W}_x\text{O}_{12}$ ($0 \leq x \leq 1$); ${}^7\text{Li}$ PFG NMR spectra of $\text{Li}_{7-2x-3y}\text{Al}_y\text{La}_3\text{Zr}_{2-x}\text{W}_x\text{O}_{12}$ ($x = 0.5$); fitting results of $\sigma(\omega)$ of $\text{Li}_{7-2x-3y}\text{Al}_y\text{La}_3\text{Zr}_{2-x}\text{W}_x\text{O}_{12}$ ($0 \leq x \leq 1$); and low-temperature properties of $\text{Li}_{7-2x-3y}\text{Al}_y\text{La}_3\text{Zr}_{2-x}\text{W}_x\text{O}_{12}$ ($0 \leq x \leq 1$) (PDF)

AUTHOR INFORMATION

Corresponding Authors

*E-mail: rfg@magnet.fsu.edu.

*Phone: 86 0592 2185 753. Fax: 86 0592 2185 753. E-mail: yyang@xmu.edu.cn.

Author Contributions

The manuscript was written through contributions of all authors. All authors have given approval to the final version of the manuscript.

Funding

The National Basic Research Program of China (973 program, Grant no. 2011CB935903) and the National Natural Science Foundation of China (Grant nos. 21233004 and 21021002, and in part 21428303).

Notes

The authors declare no competing financial interest.

ACKNOWLEDGMENTS

The authors are grateful to Dr. Vanessa K. Peterson of Bragg Institute, ANSTO, Australia, for her technical support on high-resolution NPD data collection. R.F. is also indebted to being a PCOSS fellow supported by the State Key Lab of Physical Chemistry of Solid Surfaces, Xiamen University, China.

ABBREVIATIONS

XRD, X-ray diffraction; EDS, energy-dispersive spectrometry; NPD, neutron powder diffraction; SEM, scanning electron microscopy; PFG NMR, pulse field gradient nuclear magnetic resonance; c.s., chemical shift; L.W., line width; occu, occupancy

REFERENCES

- (1) Armand, M.; Tarascon, J. M. Building Better Batteries. *Nature* **2008**, *451*, 652–657.
- (2) Goodenough, J. B.; Kim, Y. Challenges for Rechargeable Li Batteries. *Chem. Mater.* **2010**, *22*, 587–603.
- (3) Li, J.; Ma, C.; Chi, M.; Liang, C.; Dudney, N. J. Solid Electrolyte: The Key for High-Voltage Lithium Batteries. *Adv. Energy Mater.* **2015**, *5*, [10.1002/aenm.201401408](#)
- (4) Kamaya, N.; Homma, K.; Yamakawa, Y.; Hirayama, M.; Kanno, R.; Yonemura, M.; Kamiyama, T.; Kato, Y.; Hama, S.; Kawamoto, K.; Mitsui, A. A Lithium Superionic Conductor. *Nat. Mater.* **2011**, *10*, 682–686.
- (5) Cao, C.; Li, Z.; Wang, X.; Zhao, X.; Han, W. Recent Advantages in Inorganic Solid Electrolytes for Lithium Batteries. *Front. Energy Res.* **2014**, *2*, [10.3389/fenrg.2014.00025](#)
- (6) Thangadurai, V.; Narayanan, S.; Pinzaru, D. Garnet-Type Solid-State Fast Li Ion Conductors for Li Batteries: Critical Review. *Chem. Soc. Rev.* **2014**, *43*, 4714–4727.
- (7) Murugan, R.; Thangadurai, V.; Weppner, W. Fast Li Ion Conduction in Garnet-Type $\text{Li}_7\text{La}_2\text{Zr}_2\text{O}_{12}$. *Angew. Chem., Int. Ed.* **2007**, *46*, 7778–7781.
- (8) Li, Y.; Han, J.; Wang, C.; Xie, H.; Goodenough, J. B. Optimizing Li^+ Conductivity in a Garnet Framework. *J. Mater. Chem.* **2012**, *22*, 15357–15361.
- (9) Ohta, S.; Kobayashi, T.; Asaoka, T. High Lithium Ionic Conductivity in the Garnet-Type Oxide $\text{Li}_{7-x}\text{La}_3(\text{Zr}_{2-x}\text{Nb}_x)\text{O}_{12}$ ($x = 0–2$). *J. Power Sources* **2011**, *196*, 3342–3345.
- (10) Allen, J. L.; Wolfenstine, J.; Rangasamy, E.; Sakamoto, J. Effect of Substitution (Ta, Al, Ga) on the Conductivity of $\text{Li}_7\text{La}_2\text{Zr}_2\text{O}_{12}$. *J. Power Sources* **2012**, *206*, 315–319.
- (11) Dhivya, L.; Janani, N.; Palanivel, B.; Murugan, R. Li^+ Transport Properties of W Substituted $\text{Li}_7\text{La}_2\text{Zr}_2\text{O}_{12}$ Cubic Lithium Garnets. *AIP Adv.* **2013**, *3*, 082115.
- (12) Xu, M.; Park, M. S.; Lee, J. M.; Kim, T. Y.; Park, Y. S.; Ma, E. Mechanisms of Li^+ Transport in Garnet-Type Cubic $\text{Li}_{3+x}\text{La}_3\text{M}_2\text{O}_{12}$ ($\text{M} = \text{Te}, \text{Nb}, \text{Zr}$). *Phys. Rev. B: Condens. Matter Mater. Phys.* **2012**, *85*, 052301.
- (13) Awaka, J.; Takashima, A.; Kataoka, K.; Kijima, N.; Idemoto, Y.; Akimoto, J. Crystal Structure of Fast Lithium-Ion-Conducting Cubic $\text{Li}_7\text{La}_2\text{Zr}_2\text{O}_{12}$. *Chem. Lett.* **2011**, *40*, 60–62.
- (14) Han, J.; Zhu, J.; Li, Y.; Yu, X.; Wang, S.; Wu, G.; Xie, H.; Vogel, S. C.; Izumi, F.; Momma, K.; Kawamura, Y.; Huang, Y.; Goodenough, J. B.; Zhao, Y. Experimental Visualization of Li Conduction Pathways in Garnet-Type $\text{Li}_7\text{La}_2\text{Zr}_2\text{O}_{12}$. *Chem. Commun.* **2012**, *48*, 9840–9842.
- (15) Thompson, T.; Sharafi, A.; Johannes, M. D.; Huq, A.; Allen, J. L.; Wolfenstine, J.; Sakamoto, J. A Tale of Two Sites: On Defining the Carrier Concentration in Garnet-Based Ionic Conductors for Advanced Li Batteries. *Adv. Energy Mater.* **2015**, *5*, [10.1002/aenm.201500096](#)
- (16) Wang, D.; Zhong, G.; Dolotko, O.; Li, Y.; McDonald, M. J.; Mi, J.; Fu, R.; Yang, Y. The Synergistic Effects of Al and Te on the Structure and Li^+ -Mobility of Garnet-Type Solid Electrolyte. *J. Mater. Chem. A* **2014**, *2*, 20271–20279.
- (17) Liss, K.-D.; Hunter, B.; Hagen, M.; Noakes, T.; Kennedy, S. Echidna-The New High-Resolution Powder Diffractometer Being Built at OPAL. *Phys. B* **2006**, *385–386*, 1010–1012.
- (18) Toby, B. H.; Von Dreele, R. B. GSAS-II: the Genesis of a Modern Open-Source All Purpose Crystallography Software Package. *J. Appl. Crystallogr.* **2013**, *46*, 544–549.
- (19) Dean, J. A. *Lange's Hand Book of Chemistry*, fifteenth ed.; McGraw-Hill: New York, 1999.
- (20) Li, Y.; Han, J.; Wang, C.; Vogel, S. C.; Xie, H.; Xu, M.; Goodenough, J. B. Ionic Distribution and Conductivity in Lithium Garnet $\text{Li}_7\text{La}_2\text{Zr}_2\text{O}_{12}$. *J. Power Sources* **2012**, *209*, 278–281.
- (21) Xie, H.; Alonso, J. A.; Li, Y.; Fernandez-Diaz, M. T.; Goodenough, J. B. Lithium Distribution in Aluminum-Free Cubic $\text{Li}_7\text{La}_2\text{Zr}_2\text{O}_{12}$. *Chem. Mater.* **2011**, *23*, 3587–3589.
- (22) Bloembergen, N.; Purcell, E. M.; Pound, R. V. Relaxation Effects in Nuclear Magnetic Resonance Absorption. *Phys. Rev.* **1948**, *73*, 679–715.
- (23) van Wüllen, L.; Echelmeyer, T.; Meyer, H.-W.; Wilmer, D. The Mechanism of Li-Ion Transport in the Garnet $\text{Li}_5\text{La}_3\text{Nb}_2\text{O}_{12}$. *Phys. Phys. Chem. Phys.* **2007**, *9*, 3298–3203.
- (24) Fu, R.; Ma, Z.; Zheng, J. P.; Au, G.; Plichta, E. J.; Ye, C. High-Resolution ${}^7\text{Li}$ Solid-State NMR Study of $\text{Li}_x\text{V}_2\text{O}_5$ Cathode Electrodes for Li-Rechargeable batteries. *J. Phys. Chem. B* **2003**, *107*, 9730–9735.
- (25) Stejskal, E. O.; Tanner, J. E. Spin Diffusion Measurements: Spin Echoes in the Presence of a Time Dependent Field Gradient. *J. Chem. Phys.* **1965**, *42*, 288–292.
- (26) Jonscher, A. K. *Dielectric Relaxation in Solids*; Chelsea Dielectric Press: London, 1983.
- (27) Ahmad, M. M. Estimation of the Concentration and Mobility of Mobile Li^+ in the Cubic Garnet-Type $\text{Li}_7\text{La}_2\text{Zr}_2\text{O}_{12}$. *RSC Adv.* **2015**, *5*, 25824–25829.